Electrical Impedance Tomography, Enclosure Method and Machine Learning

Siltanen, Samuli

IEEE
2020-10-20

Siltanen , S & Ide , T 2020 , Electrical Impedance Tomography, Enclosure Method and Machine Learning . in PROCEEDINGS OF THE 2020 IEEE 30TH INTERNATIONAL WORKSHOP ON MACHINE LEARNING FOR SIGNAL PROCESSING (MLSP) . IEEE International Workshop on Machine Learning for Signal Processing , IEEE , International Workshop on Machine Learning for Signal Processing , Espoo , Finland , 21/09/2020 . https://doi.org/10.1109/MLSP4

http://hdl.handle.net/10138/327174
https://doi.org/10.1109/MLSP49062.2020.9231717

unspecified
acceptedVersion

2020 IEEE INTERNATIONAL WORKSHOP ON MACHINE LEARNING FOR SIGNAL PROCESSING, SEPT. 21–24, 2020, ESPOO, FINLAND

ELECTRICAL IMPEDANCE TOMOGRAPHY, ENCLOSURE METHOD AND MACHINE LEARNING

Samuli Siltanen[*]

University of Helsinki
Department of Mathematics and Statistics
PO Box 68, 00014 University of Helsinki, Finland
Samuli.Siltanen@helsinki.fi

Takanori Ide[†]

EQUOS RESEARCH CO.,LTD.
Tokyo Laboratory
Tokyo, Japan
i24824_ide@aisin-aw.co.jp

ABSTRACT

Electrical impedance tomography (EIT) is a non-destructive imaging method, where a physical body is probed with electric measurements at the boundary, and information about the internal conductivity is extracted from the data. The *enclosure method* of Ikehata [J. Inv. Ill-Posed Prob. 8(2000)] recovers the convex hull of an inclusion of unknown conductivity embedded in known background conductivity. Practical implementations of the enclosure method are based on least-squares (LS) fitting of lines to noise-robust values of the so-called *indicator function*. It is shown how a convolutional neural network instead of LS fitting improves the accuracy of the enclosure method significantly while retaining interpretability.

Index Terms— inverse problem, electrical impedance tomography, enclosure method, convolutional neural network

1. INTRODUCTION

Electrical impedance tomography (EIT) is a non-destructive imaging method. In EIT a conductive body is probed with electric measurements at the boundary, and information about the internal conductivity distribution is extracted from the data. The task of interpreting EIT data is an ill-posed inverse problem, meaning that reconstructions are extremely sensitive to modelling errors and measurement noise.

We focus on a restricted version of EIT: extracting the convex hull of inclusions embedded in constant background conductivity. By *inclusion* we mean a possibly multi-component domain of unknown conductivity. Such applications arise for example in process and construction industries [1–3]. Our methodology is based on the *enclosure method* of Ikehata [4, 5], where the asymptotics of a so-called indicator function reveal the convex hull of the inclusion set.

We introduce a novel hybrid algorithm combining traditional inversion analysis and machine learning. In ill-posed inverse problems it is not advisable to use the measured data as the input to a learning algorithm: even in very simple examples, learning the well-posed direct problem is much more efficient than learning the ill-posed inverse problem.

We propose using noise-robust inversion methods, in this case the enclosure method, for extracting stable features from the data and subsequently learning from them. We call such approaches *Robust Gray-Box* (RGB) algorithms, as the intermediate features offer more interpretability than black-box learning. In this work we show how a simple convolutional neural network (CNN) can recover the convex hull from noisy indicator function values much more accurately than the state-of-the-art least-squares algorithm. (An analogous hybrid strategy was employed in [6, 7], where blurred EIT images achieved with the *D-bar method* were sharpened with neural network models in post-processing.)

We take $\Omega \subset \mathbb{R}^2$ to be the unit disc and consider conductivities $\sigma : \Omega \to \mathbb{R}$ of the form

$$\sigma(x) = 1 + \chi_D(x)h(x). \tag{1}$$

Here $D \subset \Omega$ is the set of inclusions, and $\chi_D(x)$ equals one when $x \in D$ and zero otherwise. We take D to consist of a finite random collection of non-overlapping discs or ellipses. Further, the function $h(x)$ has a constant value, not equal to one, inside each component of D. We assume that the conductivity thus defined is bounded and strictly positive:

$$0 < M^{-1} \leq \sigma(z) \leq M. \tag{2}$$

A mathematical model for EIT was formulated by Calderón in [8]. Applying voltage f at the boundary leads to the following elliptic partial differential equation (PDE):

$$\begin{cases} \nabla \cdot \sigma \nabla u &= 0 \text{ in } \Omega, \\ u|_{\partial\Omega} &= f. \end{cases} \tag{3}$$

Here u is the electric voltage potential and $-\sigma\nabla u$ is the electric current vector field that has no sinks or sources inside Ω. The quantity $\sigma \partial u/\partial \vec{n}|_{\partial\Omega} = \sigma \vec{n} \cdot \nabla u|_{\partial\Omega}$ is the electric current

[*]Thanks to the Academy of Finland and to the Jane and Aatos Erkko Foundation for financial support.

[†]Thanks to the Academy of Finland for financial support.

978-1-7281-6662-9/20/$31.00 ©2020 IEEE

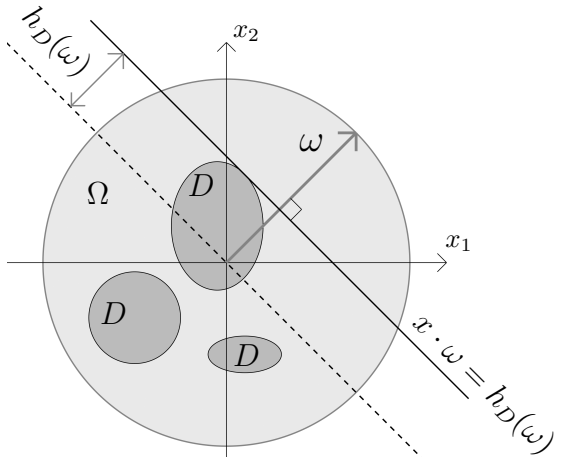

Fig. 1. Define the support function of inclusion $D \subset \mathbb{R}^2$ with direction $\omega \in S^1$ by $h_D(\omega) := \sup_{x \in D} x \cdot \omega$. Here Ω is the unit disc, and the inclusion D has three elliptical components.

density along the boundary, where $\vec{n}$ is the outward normal vector field on $\partial\Omega$. The *Dirichlet-to-Neumann (DN) map*

$$\Lambda_\sigma : f \mapsto \sigma \frac{\partial u}{\partial \vec{n}}|_{\partial\Omega} \tag{4}$$

is an ideal infinite-precision model for the set of all possible static voltage-to-current boundary measurements. For more advanced EIT data models we refer to [9].

Define the support function of the inclusion $D \subset \mathbb{R}^2$, with direction specified by a unit vector $\omega \in S^1$, by

$$h_D(\omega) := \sup_{x \in D} x \cdot \omega. \tag{5}$$

See Figure 1 for an illustration. Ikehata showed in [4] how to use Λ_σ to calculate a so-called *indicator function* $I_\omega(\tau)$, which in turn determines $h_D(\omega)$. The knowledge of $h_D(\omega)$ for all directions ω gives the convex hull of D.

Denote by $\omega^\perp$ the vector ω rotated counterclockwise by angle $\pi/2$. Then $\omega \cdot \omega^\perp = 0$. For each $\tau > 0$ and $x \in \mathbb{R}^2$ define the exponential function

$$f_\omega(x, \tau) := e^{\tau x \cdot \omega + i \tau x \cdot \omega^\perp}. \tag{6}$$

The indicator function $I_\omega(\tau)$ is defined by

$$I_\omega(\tau) = \int_0^{2\pi} \big((\Lambda_\sigma - \Lambda_1) \overline{f_\omega(\,\cdot\,, \tau)|_{\partial\Omega}} \big)(\theta) f_\omega(e^{i\theta}, \tau)\, d\theta, \tag{7}$$

where Λ_1 is the DN map of the constant conductivity with value 1 (also known as the *dummy load*). The large-τ asymptotics of $I_\omega(\tau)$ reveal the support function:

$$h_D(\omega) = \lim_{\tau \longrightarrow \infty} \frac{\log |I_\omega(\tau)|}{2\tau}. \tag{8}$$

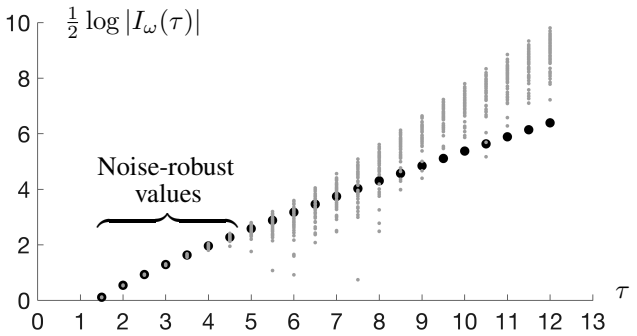

Fig. 2. The effect of measurement noise on the indicator function. Larger (black) dots show the actual values $\frac{1}{2} \log |I_\omega(\tau)|$. We calculate the Dirichlet-to-Neumann maps as finite matrices as explained in [13, Section 13.2]. Then we added simulated random white noise with realistic amplitude to the matrix elements. The smaller (grey) dots show the same τ-values calculated with formula (7) from noisy Dirichlet-to-Neumann matrices with 50 different realizations of random noise. We conclude that the computation is relatively robust against noise for $\tau \leq 4.5$.

However, in practice the measurement noise typically corrupts the computed values of $I_\omega(\tau)$ for $\tau > 4.5$. See Figure 2 for an illustration of the effects of noise. Therefore, it is not plausible to take τ large enough for the asymptotics in (8) to kick in. Rather, some estimation of the slope of the function $\log |I_\omega(\tau)|$ for small values of τ has been used [10–12].

In this work we demonstrate how a convolutional neural network can learn the correspondence between small-τ values of $I_\omega(\tau)$ and the support function. The paper is organized as follows. In Section 2 we present the classical least-squares fit method. Section 3 is devoted to the CNN-based inversion. We conclude our results in Section 4.

2. LEAST-SQUARES FITTING

We recover the support function approximately using the following least-squares approach. We define $N = 45$ directions uniformly distributed over the whole 2π range:

$$\begin{aligned} \omega_j &= [\cos\theta_j, \sin\theta_j]^T, \\ \theta_j &= 2\pi(j-1)/N, \qquad j = 1, \ldots, N. \end{aligned} \tag{9}$$

Further, τ ranges in the interval from 1.5 up to 4.5 with step size 0.5:

$$\tau_\ell = 1 + \frac{\ell}{2}, \qquad \ell = 1, 2, \ldots, 7. \tag{10}$$

For each fixed direction ω_j we fit a line to the planar points

$$(\tau_\ell, \frac{1}{2} \log |I_{\omega_j}(\tau_\ell)|) \in \mathbb{R}^2, \qquad \ell = 1, 2, \ldots, 7$$

in the least-squares sense. According to the asymptotic formula (8), the slope of the fitted line approximates the support function of the inclusion in direction ω_j.

The inversion process is illustrated in Figure 3. We aim to recover the convex hull of an inclusion consisting of two lower-than-background discs. The LS fit consistently overestimates the support function, leading to the reconstructed set being a lot larger than the convex hull of the inclusion. Given the systematic overshoot of the fitted slope, one could think that a simple correction would improve the method.

However, applying the same approach to a more complicated inclusion, having both low- and high-conductivity components, leads to both too small and too large reconstructed support function values. See Figure 4. The least-squares fit sometimes underestimates the slope, leading to false negative classifications of points.

See also Figures 8 and 7, as well as Table 1, for results.

3. CONVOLUTIONAL NEURAL NETWORK

Learning the approximate convex hull from indicator function values is a straightforward task to define for a neural network model. The input data consists of 7×45 numbers:

$$\frac{1}{2}\log|I_{\omega_j}(\tau_\ell)|,$$

where the seven values of τ_ℓ are defined in (10) and the 45 directions ω_j are given in (9). The output is 45 real numbers, namely approximate $h_D(\omega_j)$ for $j = 1, \ldots, N$.

We wish to use CNN with two-dimensional filters, so we organize the input in the form of an image. There are 21 rows and 50 columns. Each column corresponds to a fixed direction; the first 45 columns are directions from 1 to 45 and columns 46–50 are copies of columns 1–5. The repetition is for allowing the convolution to analyse the relation between consecutive angles 43,44,45,1,2,3 (note periodicity in the directions evident in formula (9)) in an analogous way to angles in the middle of the range.

Each column has the seven indicator function values multiply listed in this order:

$$1, 2, 3, 4, 5, 6, 7, 7, 6, 5, 4, 3, 2, 1, 1, 2, 3, 4, 5, 6, 7.$$

The multiplicity is for avoiding problems with boundary effects coming from the (three pixel wide) zero padding.

We use the following CNN architecture in this work. There are six layers:

Image Input	21x50 images, zero mean
Convolution	120 filters of size 6x4,
Leaky ReLU	Leaky ReLU with scale 0.01
Fully Connected	Fully connected layer, 45 outputs
Tanh	Hyperbolic tangent layer
Regression Output	45 outputs

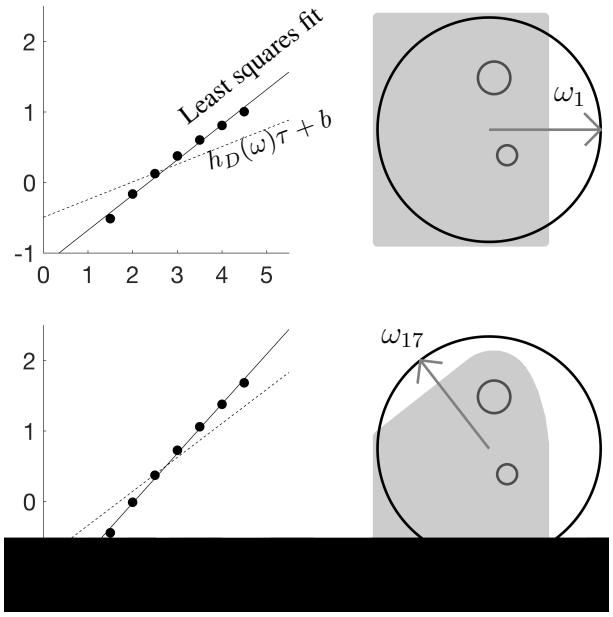

Fig. 3. Performance of least-squares fitting in a simple case of two lower-than-background disc inclusions.The estimated slope is systematically larger than the actual support function; this leads to consistently thick reconstruction of the convex hull. In other words, there are plenty of false positives but no false negatives in the resontructed set.

We used three-pixel zero padding in the convolutional layer. The computation was implemented in Matlab R2019a Deep Learning Toolbox.

3.1. Simulated training, validation and testing datasets

Disc inclusions. For training and validation data we create 19 000 different conductivities, each with minimum of one and maximum of four disc inclusions. The homogeneous background conductivity is equal to 1. The randomly placed disc inclusions have these statistics:

- Random radii uniformly distributed in $[0.05,\ 0.2]$.
- The conductivity inside each inclusion is random with uniform distribution in either $[1.5,\ 5]$ (higher than background) or in $[0.2,\ 0.67]$ (lower than background).

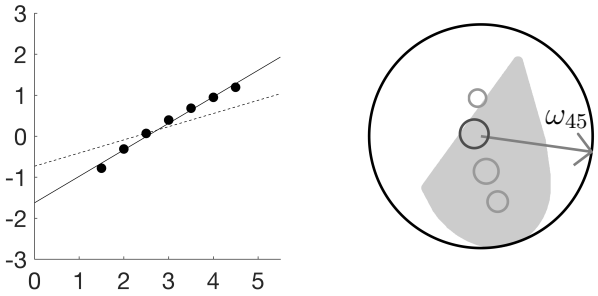

Fig. 4. Performance of least-squares fitting in a case of four disc inclusions with three higher and one lower conductivity than background. The estimated slope is sometimes larger and sometimes smaller than the actual support function. As a result, there are both false positives and false negatives in the reconstructed set. Compare to Figure 3.

The choice between higher or lower was made for each inclusion independently with probability $1/2$.

- The discs in a fixed conductivity example are disjoint and at least a distance of 0.1 away from the unit circle.

Elliptic inclusions. For testing the performance of the network model, we generated 1 000 random conductivities, each having 5 having elliptic inclusions. The homogeneous background conductivity is equal to 1. The randomly placed and oriented elliptic inclusions have these statistics:

- Each semi-major axis is random with half-length R uniformly distributed in the interval $[0.04,\ 0.22]$.

- Each semi-minor axis is random with half-length r uniformly distributed in the interval $[0.04, R]$.

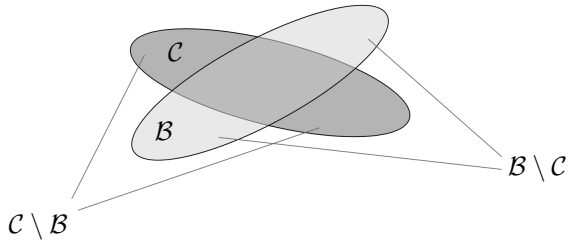

Fig. 5. Quantitative measurement of the quality of reconstructed convex hulls. We calculate the area of the false negative set $\mathcal{C} \setminus \mathcal{B}$ and false positive set $\mathcal{B} \setminus \mathcal{C}$ into (11).

- The conductivity inside each elliptic inclusion is random with uniform distribution in either $[1.3,\ 7]$ (higher than background) or in $[0.14,\ 0.77]$ (lower than background). The choice between higher or lower was made for each inclusion independently with probability $1/2$.

- The ellipses in a fixed conductivity example are disjoint and at least a distance of 0.1 away from the unit circle.

The set of elliptic inclusions generalize the set of discs in several ways. There are more inclusions (5 ellipses, at most 4 discs), the ellipses may have larger diameters than the discs, and the conductivity values in elliptic inclusions vary in a wider range than for discs.

3.2. Measuring the quality of reconstructions

Denote the true convex hull by $\mathcal{C} \subset \mathbb{R}^2$ and the reconstructed convex hull by $\mathcal{B} \subset \mathbb{R}^2$. We use the relative error

$$\frac{|\mathcal{C} \setminus \mathcal{B}| + |\mathcal{B} \setminus \mathcal{C}|}{|\Omega|} \cdot 100\%, \tag{11}$$

where $|\ \cdot\ |$ is area. Here $|\Omega| = \pi$ since we work in the unit disc. See Figure 5 for an illustration.

3.3. Results

Our training set consisted of 16000 cases, out of which 6900 had a random number of disc inclusions (at least one and at most four), and 9100 had four disc inclusions. The larger share of four-inclusion examples allows training the network more on the most difficult cases.

Our validation set consists of 3000 cases with a random number of disc inclusions (at least one and at most four).

We trained the CNN for 2000 epochs of 125 iterations each. We used a constant learning rate of 0.01, and we validated every 30 iterations. The training took 764 minutes on a desktop Mac CPU, and the final RMSE was 0.15. See Figure 6 for the RMSE and loss during training. See Table 1 and the bottom plot in Figure 7 for reconstruction quality, and Figure 8 for examples of reconstructions.

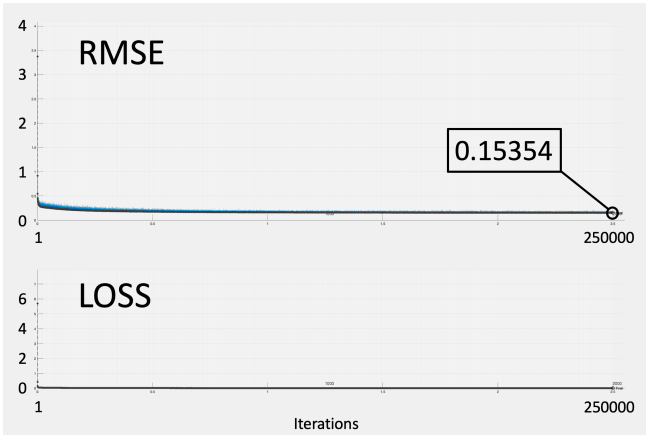

Fig. 6. RMSE and loss during training. The iterations run from 1 to 250000. The final RMSE was 0.15.

Table 1. Statistics of the relative error (11) for 1000 test cases. See Figure 7 for histograms and Figure 8 for interesting special cases of reconstructions.

	Mean	*Median*	*Max*
Least-squares fit	28.3%	27.6%	53.7%
CNN	4.2%	3.8%	14.8%

4. DISCUSSION AND CONCLUSIONS

CNNs are clearly better than least-squares line fitting methods in capturing the nonlinear relationship between small-τ indicator function values and convex hulls of inclusions. The error statistics in Table 1 and Figure 7, and the illustrated reconsrtuctions in Figure 8, show significant quantitative advantage of machine learning over the classical approach. Curiously, in only one case out of 1000 did the LS fit outperform the CNN; see Figure 8(d).

We found the CNN specified in Section 3 by trial and error. Deeper designs with more layers did not seem to improve the results, and pooling resulted in poorer performance in our tests. However, there is no reason to believe that the network architecture used in this work would be optimal; there must exist another neural network model that reduces the reconstruction error further. That being said, we find it positive that a very simple CNN architecture is able to improve reconstruction quality as much as reported in Table 1.

As future research directions we see implemention the method with more realistic data models such as the complete electrode model, and extension to generalized enclosure-type probing with different shapes such as cones, discs and parabola [14–17]. Also, the noisy indicator function values shown in Figure 2 seem to have a systematic bias. Perhaps they could be used to an advantage in a machine learning approach?

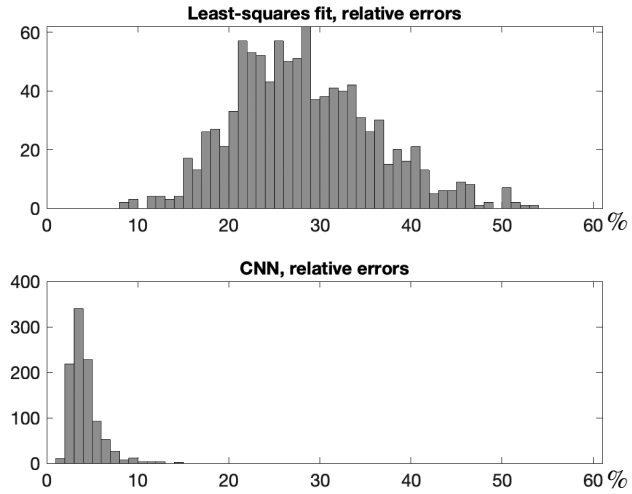

Fig. 7. Comparison of the accuracy of the classical least-square fit method and the new machine-learning approach for 1000 test cases. The relative error is defined in formula (11). See also Table 1.

5. REFERENCES

[1] LM Heikkinen, J Kourunen, T Savolainen, PJ Vauhkonen, JP Kaipio, and M Vauhkonen, "Real time three-dimensional electrical impedance tomography applied in multiphase flow imaging," *Measurement Science and Technology*, vol. 17, no. 8, pp. 2083, 2006.

[2] MA Bennett and Richard A Williams, "Monitoring the operation of an oil/water separator using impedance tomography," *Minerals Engineering*, vol. 17, no. 5, pp. 605–614, 2004.

[3] Milad Hallaji, Aku Seppänen, and Mohammad Pour-Ghaz, "Electrical resistance tomography to monitor unsaturated moisture flow in cementitious materials," *Cement and Concrete Research*, vol. 69, pp. 10–18, 2015.

[4] M Ikehata, "Reconstruction of the support function for inclusion from boundary measurements," *Journal of Inverse and Ill-Posed Problems*, vol. 8, pp. 367–378, 2000.

[5] M Ikehata, "How to draw a picture of an unknown inclusion from boundary measurements. Two mathematical inversion algorithms," *Journal of Inverse and Ill-Posed Problems*, vol. 7, no. 3, pp. 255–271, 1999.

[6] Sarah Jane Hamilton and Andreas Hauptmann, "Deep d-bar: Real-time electrical impedance tomography imaging with deep neural networks," *IEEE transactions on medical imaging*, vol. 37, no. 10, pp. 2367–2377, 2018.

[7] Sarah J Hamilton, Asko Hänninen, Andreas Hauptmann, and Ville Kolehmainen, "Beltrami-net: domain-independent deep d-bar learning for absolute imaging with electrical impedance tomography (a-eit)," *Physiological measurement*, vol. 40, no. 7, pp. 074002, 2019.

[8] A.-P. Calderón, "On an inverse boundary value problem," in *Seminar on Numerical Analysis and its Applications to Continuum Physics (Rio de Janeiro, 1980)*, pp. 65–73. Soc. Brasil. Mat., Rio de Janeiro, 1980.

[9] M. Cheney, D. Isaacson, and J. C. Newell, "Electrical impedance tomography," *SIAM Review*, vol. 41, no. 1, pp. 85–101, 1999.

[10] Masaru Ikehata and Samuli Siltanen, "Numerical method for finding the convex hull of an inclusion in conductivity from boundary measurements," *Inverse Problems*, vol. 16, no. 4, pp. 1043, 2000.

[11] M. Brühl and M. Hanke, "Numerical implementation of two non-iterative methods for locating inclusions by impedance tomography," *Inverse Problems*, vol. 16, pp. 1029–1042, 2000.

[12] M Ikehata and T Ohe, "A numerical method for finding the convex hull of polygonal cavities using the enclosure method," *Inverse Problems*, vol. 18, no. 1, pp. 111, 2002.

[13] J. L. Mueller and S. Siltanen, *Linear and Nonlinear Inverse Problems with Practical Applications*, SIAM, Philadelphia, PA, 2012.

[14] T Ide, H Isozaki, S Nakata, S Siltanen, and G Uhlmann, "Probing for electrical inclusions with complex spherical waves," *Communications on Pure and Applied Mathematics*, vol. 60, no. 10, pp. 1415–1442, 2007.

[15] T Ide, H Isozaki, S Nakata, and S Siltanen, "Local detection of three-dimensional inclusions in electrical impedance tomography," *Inverse problems*, vol. 26, no. 3, pp. 035001, 2010.

[16] Masaru Ikehata and Samuli Siltanen, "Electrical impedance tomography and mittag-leffler's function," *Inverse Problems*, vol. 20, no. 4, pp. 1325, 2004.

[17] GUNTHER Uhlmann and JN Wang, "Complex geometrical optics solutions and reconstruction of discontinuities," *SIAM J. Appl. Math*, vol. 68, pp. 1026–1044, 2008.

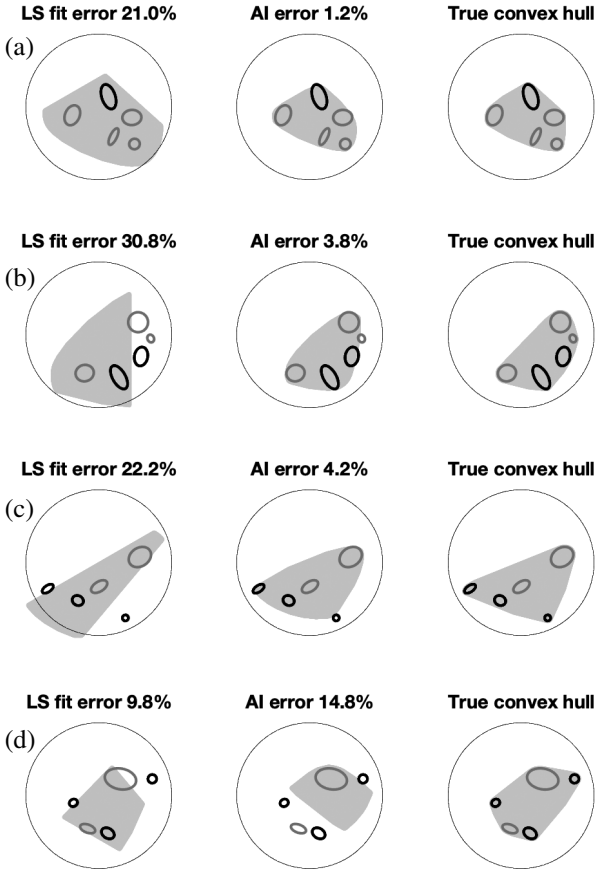

Fig. 8. Four conductivities, marked (a), (b), (c) and (d), picked out of the set of 1000 five-inclusion test cases. Case (a) represents the minimal error produced by the CNN, case (b) the median error produced by the CNN, and case (c) the mean error produced by the CNN. Curiously, case (d) is the only one out of the 1000 tests, where the least-square fit method gave a *better* result than the CNN. *Left column:* Reconstructions of convex hulls using the classical least-square fit method. *Middle column:* new CNN-based machine-learning approach. *Right column:* Ground truth, namely the approximate convex hull determined by the 45 directions used. In all images the lighter elliptical inclusions have a higher constant conductivity than background, while darker ones have lower conductivity.